Intermetallics 116 (2020) 106652

Contents lists available at ScienceDirect

Intermetallics

journal homepage: http://www.elsevier.com/locate/intermet

Gum-like mechanical behavior of a partially ordered $Al_5Nb_{24}Ti_{40}V_5Zr_{26}$ high entropy alloy

S. Zherebtsov [a], N. Yurchenko [a,*], E. Panina [a], M. Tikhonovsky [b], N. Stepanov [a]

[a] Laboratory of Bulk Nanostructured Materials, Belgorod National Research University, Belgorod, 308015, Russia
[b] National Science Center "Kharkov Institute of Physics and Technology" NAS of Ukraine, Kharkov, 61108, Ukraine

ARTICLE INFO

Keywords:
High-entropy alloys
Mechanical properties
Order/disorder transformation
Plastic deformation mechanisms
Work–hardening
Microstructure

ABSTRACT

Microstructure and mechanical behavior of a new bcc $Al_5Nb_{24}Ti_{40}V_5Zr_{26}$ high-entropy alloy in the as-cast, cold-rolled and recrystallized conditions were studied. In the as-cast condition, the $Al_5Nb_{24}Ti_{40}V_5Zr_{26}$ alloy had a single bcc phase coarse-grained (~80 μm) structure. After cold rolling to a total thickness strain 80% the alloy demonstrated typical of deformed metals tensile behavior with a short hardening stage and early necking. Annealing at 800 °C resulted in recrystallization of the matrix and formation of a small fraction of C14 type Laves phase particles. After annealing at 1100 °C, a partial B2 ordering of the matrix phase was found. In the annealed condition, the alloy showed some typical of gum metals features associated with low work hardening and large elongation. The manifestation of a gum-like behavior can be ascribed to the formation of dislocation channels due to the local disordering of the bcc matrix in shear planes. In addition, an unusual (inverse) dependence of yield strength on the recrystallized grain size was observed, most possibly due to a different degree of ordering of the matrix phase.

1. Introduction

High-entropy alloys (HEAs) constitute a new class of metallic materials attracting increased attention due to an unusual combination of mechanical and functional characteristics [1–6]. The initial idea strongly emphasized maximizing configurational entropy by taking multiple principle elements in equiatomic proportions to obtain random solid solution structures [1]. However, high configurational entropy per se was found to be not a sufficient requirement for the solid solutions formation [7,8]; therefore the formation of intermetallic phases or ordering can frequently be observed in such multicomponent alloys [4,9]. Thus, current research efforts are mainly focused on the development of new compositions with properties superior to the conventional alloys based on a single element [4,5,10,11]. As such, there are no strict requirements for chemical and phase compositions of the potential HEAs anymore; new alloys composed of several phases (including intermetallic compounds or ordered phases) are considered as well [4]. Nevertheless, there are some HEAs with surprisingly stable solid solution structures which, in addition, demonstrate unusual and attractive properties.

The best-known examples of single solid solution phase HEAs are CoCrFeMnNi system alloys. These alloys tend to possess a single face-centered cubic (fcc) structure and exhibit superior strength, ductility, and toughness at cryogenic temperature [3,7,12,13]. Although the mechanical behavior of the CoCrFeMnNi alloys, in general, resembles that of austenitic (fcc) steels [14,15], the multicomponent nature of the fcc solid solutions gives rise to various effects not typical of conventional alloys. For example, complex configuration of the dislocation cores or strong variations in the stacking fault energy were reported for some HEAs [16,17]. Besides, the existence of ordering in this system alloys is a point of contention [18,19]; specifically, there are some claims that the existence of short-range order can affect the mechanical behavior [20].

Another well-known single-phase HEA example is the TiZrHfNbTa alloy based on refractory elements (RHEA); this alloy with a body-centered cubic (bcc) solid solution structure was initially suggested for high-temperature applications [21,22]. Deformation of the TiZrHfNbTa alloy studied at room temperature [23,24] was found to be controlled by the glide of screw dislocations and the formation of dislocation bands acting as long-range obstacles. It was also revealed that partial ordering, caused by proper heat treatment and/or additional alloying can cause drastic changes in the mechanical behavior of the TiZrHfNbTa or similar alloys [25,26].

* Corresponding author. Laboratory of Bulk Nanostructured Materials, Belgorod National Research University, Pobeda 85, Belgorod, 308015, Russia.
E-mail address: yurchenko_nikita@bsu.edu.ru (N. Yurchenko).

https://doi.org/10.1016/j.intermet.2019.106652
Received 8 August 2019; Received in revised form 14 October 2019; Accepted 2 November 2019
Available online 8 November 2019

Mechanical behavior of the TiZrHfNbTa RHEA is in turn somehow close to that of certain beta (bcc) titanium alloys. For example, this HEA demonstrated high strength and very low work hardening during cold rolling [27] implying some similarities with gum metals, which are a specific class of beta titanium alloys that exhibit unusual mechanical behavior including superelasticity, high strength and ductility, low modulus, Invar and Elinvar effects [28]. The gum-like metastable Ti alloys consist of group IVa and Va elements and oxygen [28] (typical examples are (at.%): Ti – 20Nb – 3.5Ta – 3.4Zr – 1.2O or Ti – 12Ta – 9Nb – 3 V – 6Zr – 1.5O), i.e. resembling the above mentioned RHEA composition. The mechanical behavior of this gum alloys is basically ascribed to the development of deformation along certain crystallographic planes with low resistance to shear [28–30]. Initially, dislocation activity was considered to be inhibited by Zr–O atoms clusters and the operating deformation mechanism was associated with the development of ideal bulk shear or giant faults. Although later dislocation and twining activity was reported in gum metals [e.g. Refs. [31,32]], some features of gum metals can rather be related to martensitic transformation effects [33–35].

Despite some similarities in mechanical behavior, it is still unclear to what extent the bcc RHEAs can behave like gum metals. In this work, we introduce a new nearly single-phase $Al_5Nb_{24}Ti_{40}V_5Zr_{26}$ HEA. Detailed microstructure characterization following uniaxial tension and cold rolling deformation experiments of the $Al_5Nb_{24}Ti_{40}V_5Zr_{26}$ HEA was done to provide a comprehensive understanding of microstructure evolution and deformation behavior of this alloy. We demonstrate that the mechanical characteristics of the alloy are dependent on the ordered nature of the matrix.

2. Materials and methods

The alloy with a nominal composition of $Al_5Nb_{24}Ti_{40}V_5Zr_{26}$ (the subscripts indicate the atomic percent of the corresponding element) was produced by arc melting of the elements in a low-pressure, high-purity argon atmosphere inside a water-cooled copper cavity. The purities of the alloying elements were no less than 99.9 at.%. The size of the produced ingot was $\sim 10 \times 14 \times 50\ mm^3$. The chemical composition of the alloy measured by energy dispersive spectroscopy (EDS) closely corresponded to the nominal chemical composition.

Rectangular samples measured $8 \times 10 \times 20\ mm^3$ were cut by electric discharge machine from the as-cast ingot to carry out thermomechanical processing. Unidirectional multipass rolling using a fixed rolling speed of 30 mm/s at room temperature to a total thickness strain 80% was performed in air using a reduction per pass of approximately 0.1–0.2 mm. The rolling strain was calculated from the thickness of produced specimens. After rolling to the final thickness, some specimens were further annealed at 600, 700, 800, 900, 1000, 1100, or 1200 °C for 1 h. Prior to annealing, the samples were sealed in vacuumed (10^{-2} torr) quartz tubes filled with titanium chips to prevent oxidation. For annealing, the specimens were placed in a preheated furnace and held for a required period of time. After annealing, the specimens were water quenched. To obtain additional information, some specimens annealed at 800 °C and 1100 °C for 1 h were then rolled to a thickness reduction of 7%.

The microstructure of the alloy was examined using X-ray diffraction analysis (XRD), scanning (SEM), and transmission (TEM) electron microscopy. The XRD analysis was performed using a RIGAKU diffractometer with CuKα radiation. SEM specimens were prepared by careful mechanical polishing. SEM back-scattered electron (BSE) images of microstructures were obtained using a FEI Quanta 600 FEG microscope equipped with an EDS detector. SEM-BSE images were used for estimation of the average grain size by means of the linear intercept method with a Digimizer Image Analysis Software. The same software was used for the recrystallized fraction evaluation.

TEM examinations were performed in a mid-thickness of the rolled specimens. Samples for TEM analysis were prepared by a conventional twin-jet electropolishing at a temperature of - 35 °C and an applied voltage of 29.5 V in a mixture of 600 ml of methanol, 360 ml of butanol, and 60 ml of perchloric acid. TEM investigations were performed using a JEOL JEM-2100 microscope at an accelerating voltage of 200 kV and equipped with an EDS detector At least ten TEM bright-field images were used for evaluation of the size and volume fraction of second phase particles with the aid of the Digimizer Image Analysis Software. The TEM-EDS detector was used for measuring the chemical composition of the second phase particles; at least ten individual measurements were carried out.

The density of the alloy was measured by hydrostatic weighting method. The density was measured on specimens with dimensions $6 \times 4 \times 4\ mm^3$; 3 samples of the alloy were measured.

Specimens with the gauge dimensions of $6 \times 3 \times 1\ mm^3$ were used for mechanical tests which consisted in tension at a constant crosshead speed of $10^{-4}\ s^{-1}$ to fracture. The longitudinal axis of the specimens was aligned with the rolling direction. Elongation to fracture was determined by the measurements of spacing between marks designating the gauge length (before and after the test). At least two samples in each condition were tested. The microhardness of the specimens was examined using Vickers microhardness testing with a load of 0.3 kg. The hardness values were averaged over at least 20 individual measurements for each data point.

The equilibrium phase diagram was constructed using a Thermo-Calc (version 2019b) software and a TCHEA3 (high-entropy alloys) database.

3. Results

The density of the alloy was $6.05 \pm 0.03\ g/cm^3$. According to X-ray diffraction (XRD) data, the alloy in the as-cast condition had a single-phase bcc structure with the lattice parameter of 0.3350 ± 0.0002 nm (Fig. 1a). The microstructure of the alloy in the as-cast condition consisted of mainly equiaxed grains with a size of $d \approx 80$ μm in accordance with scanning electron microscopy (SEM) image taken in backscattered electron (BSE) diffraction mode (Fig. 1b).

After cold rolling (CR) to a thickness strain $\varepsilon_{th} = 80\%$ the alloy remained in the single-phase condition according to XRD analysis (Fig. 1a). Transmission electron microscopy (TEM) examination of the cold rolled specimens also showed the single-phase bcc structure contained irregularly distributed dislocation pile-ups (Fig. 1c).

Complete recrystallization of the cold-rolled alloy can be attained after annealing for an hour at temperatures $T \geq 700$ °C (Fig. 2). Annealing at 600 °C resulted in a partially recrystallized microstructure (recrystallized volume $V_{rec} = 39.6\%$); the size of new grains in the recrystallized areas varied from ~1.5 to ~9 μm with the mean value of 2.1 ± 1.4 μm (Fig. 2a). Some microstructure heterogeneity associated with a noticeable grain size variation in different areas (from ~6 to ~ 30 μm) was also observed after annealing at 700 °C (Fig. 2b). An increase in the annealing temperature to $T \geq 800$ °C led to the formation of a coarser and more homogeneous microstructure. It should be noted also that the coarsening rate was quite low in the interval 700–900 °C, but considerably rose at $T > 900$ °C (Fig. 2h). After annealing at 1200 °C for 1 h the grain size was 295 ± 70 μm (Fig. 2g and h).

Microstructure analysis of specimens annealed at 800 or 1100 °C, i.e. at temperatures corresponded to the intervals with different grain growth rates (Fig. 2h), suggested that the slow grain coarsening during annealing at 700–900 °C can be associated with the pinning effect from very small (~120 nm) ZrNbV-type (C14) Laves phase particles (Fig. 3a). The formation of the Laves phase was confirmed by the XRD analysis (Fig. 1a). The fraction of Laves particles was below 1% per TEM analysis. In the alloy annealed at 1100 °C a single phase microstructure was formed (Fig. 3b). However, the selected area diffraction pattern (SAED) revealed the presence of very faint reflexes which can imply partial B2 ordering of the bcc structure (outlined reflex (100) at the insert in Fig. 3b). The presence of superstructure reflections was revealed for both the CR to $\varepsilon_{th} = 80\%$ or recrystallized at 800 °C conditions neither

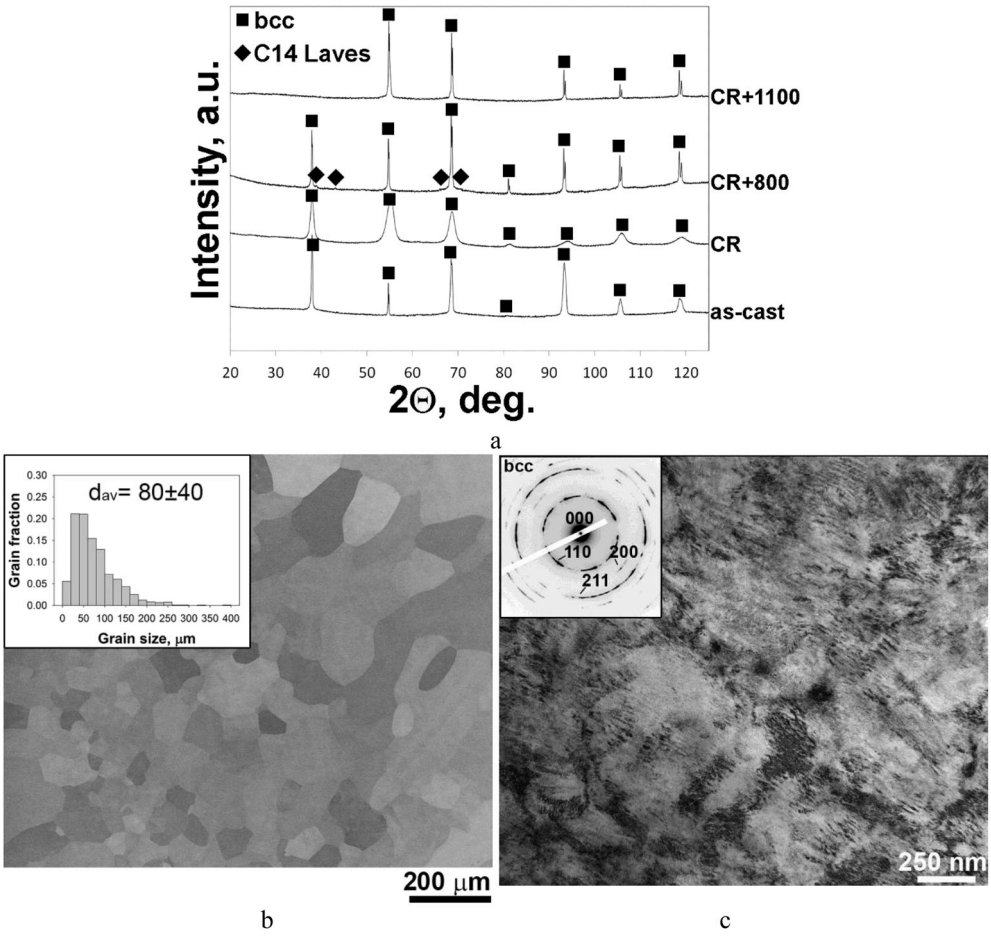

Fig. 1. XRD patterns of the $Al_5Nb_{24}Ti_{40}V_5Zr_{26}$ alloy in the as cast, cold-rolled or recrystallized conditions (a); SEM-BSE image of the alloy in the as-cast condition (b) and TEM-bright field image of the alloy after cold rolling to $\varepsilon_{th} = 80\%$ (c).

by TEM (Figs. 1c and 3a) nor by XRD (Fig. 1a). The absence of superlattice reflections on the XRD pattern of the annealed at 1100°C condition (Fig. 1a) could most probably be ascribed to low "degree of ordering".

Microhardness of the alloy non-monotonically changed with the annealing temperatures (Fig. 4a). While the annealing temperature increased to 700 °C the microhardness expectably decreased to the as-cast condition level (~300 HV). However, the further rise of the annealing temperature till 1100 °C yielded a considerable increase in the microhardness value to ~360 HV which was even higher than the microhardness of the CR condition. At the maximum annealing temperature (1200 °C) the microhardness dropped again to the level typical of the as-cast condition.

Engineering stress - engineering strain curves of the CR and annealed $Al_5Nb_{24}Ti_{40}V_5Zr_{26}$ alloy and some corresponding mechanical characteristics are shown in Fig. 4b and Table 1. The CR condition demonstrated typical of largely deformed metallic materials behavior with a short strain hardening stage and early necking. In contrast, the alloy recrystallized at 800 °C exhibited, after attaining the yield point, some decrease in flow stress with strain and relatively high uniform elongation of ~0.22. Annealing at 1100 °C resulted in a similar behavior with a slightly higher value of the yield stress in comparison to that attained after annealing at 800 °C (875 and 835 MPa, respectively) that is in agreement with the results of microhardness measurement (Fig. 4a). However the alloy after annealing at 1100 °C became softer with strain in comparison to the alloy annealed at 800 °C. Ductility of these two annealed (at 800 or 1100 °C) conditions was found to be rather close to each other.

Work hardening $\theta = d\sigma/d\varepsilon$ of all studied specimens showed a sharp decrease at small strains $\varepsilon \approx 0.01$ for the recrystallized or $\varepsilon \approx 0.025$ for the deformed conditions. During further deformation till $\varepsilon \approx 0.16$ the alloy recrystallized at 800 °C shows stable work hardening $\theta \approx 1100$ MPa while in the condition obtained by annealing at 1100 °C θ increased with strain from ~300 MPa to ~800 MPa.

The observed increase in yield stress with increasing the annealing temperature in the interval 800–1100 °C (and in the interval 700–1100 °C in the case of microhardness) resulted in a quite unusual response of yield strength to the grain size increase, associated with a negative slope of the YS-$d^{-1/2}$ dependence (Fig. 4d). This is an unusual finding since generally metals and alloys become softer with grain coarsening due to weaker Hall-Petch strengthening [36]. Since the alloy contained the Laves phase particles after the low-temperature annealing only, the observed deviation from the normal Hall-Petch strengthening was obviously not associated with precipitation strengthening.

To gain insight the observed mechanical behavior, microstructure analysis was conducted. TEM images of the specimens annealed at 800 °C for 1 h and then CR to $\varepsilon_{th} = 7\%$ showed the formation of a typical of deformed bcc alloys microstructure consisted of loose dislocation arrays along mainly one crystallographic direction (Fig. 5 a, b). Numerous individual dislocations can be observed in the areas between the arrays. All the observed dislocations, identified by the usual extinction rules, were found to possess a typical of the bcc structure Burgers vector $b = \pm a/2\langle 1\bar{1}1\rangle$. Screw dislocations crossing each other in slip bands created a kind of a dislocation network. The presence of second phase particles did not have a noticeable effect on dislocation microstructure.

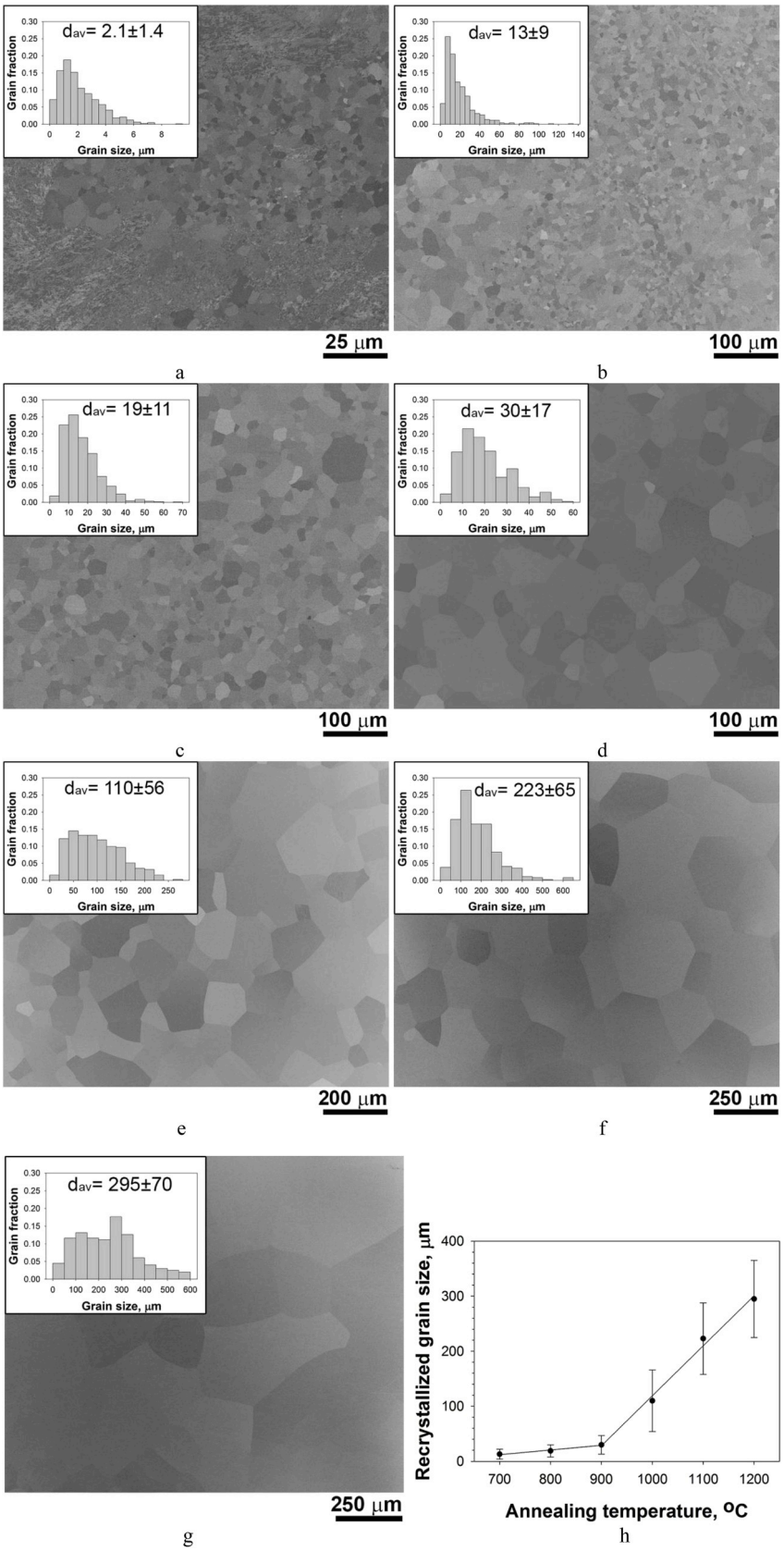

Fig. 2. SEM-BSE images the $Al_5Nb_{24}Ti_{40}V_5Zr_{26}$ alloy after cold-rolling to $\varepsilon_{th} = 80\%$ and annealing at 600 (a), 700 (b), 800 (c), 900 (d), 1000 (e), 1100 (f) or 1200 °C (g) for 1 h and grain size as a function of annealing temperature (h). Inserts in (a–g) shows the grain size distribution function and average grain size.

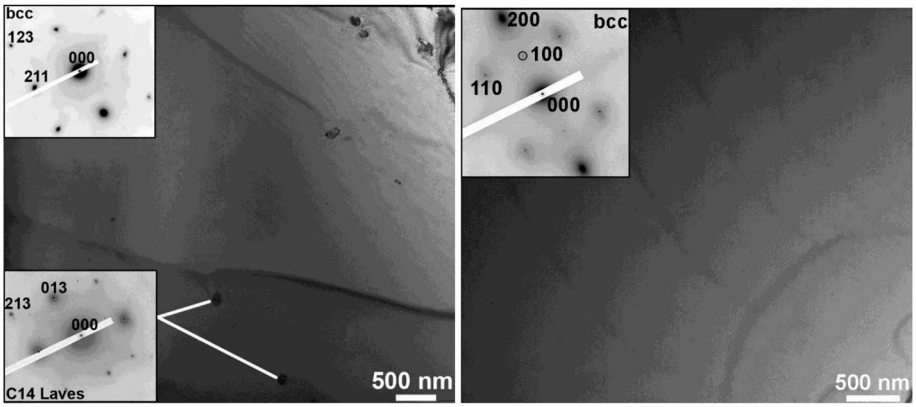

Fig. 3. TEM-bright field images of the $Al_5Nb_{24}Ti_{40}V_5Zr_{26}$ alloy after CR to $\varepsilon_{th} = 80\%$ and further annealing at 800 °C (a) or 1100 °C (b) for 1 h.

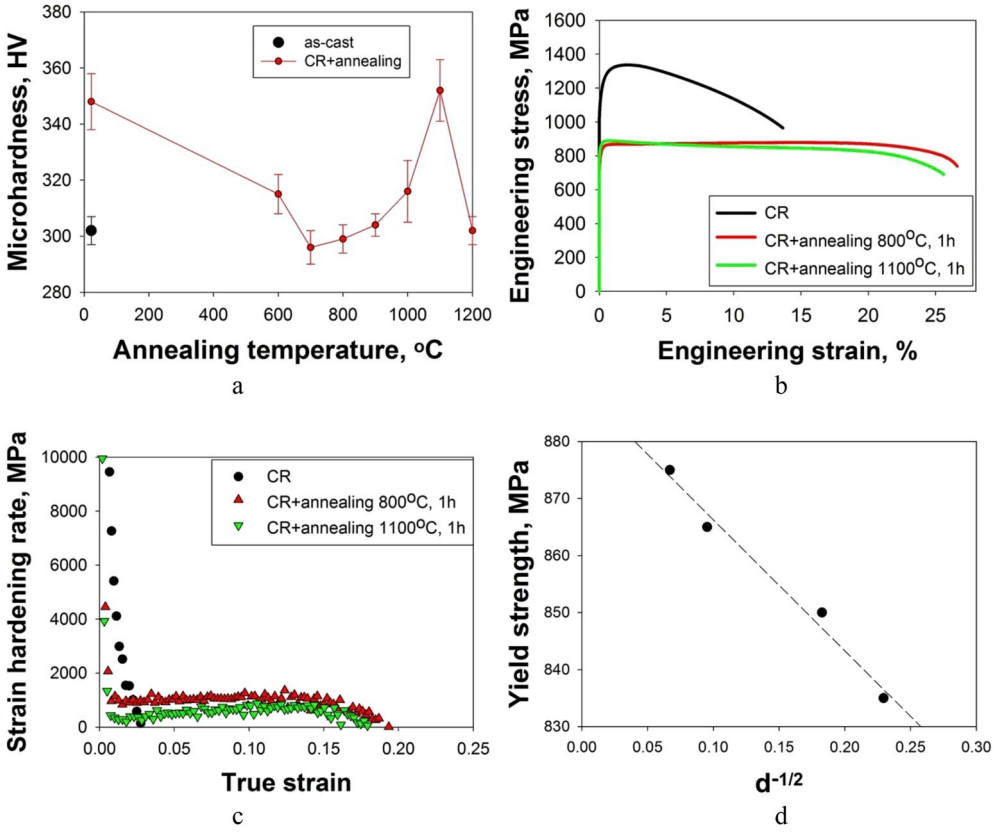

Fig. 4. Mechanical behavior of the $Al_5Nb_{24}Ti_{40}V_5Zr_{26}$ alloy in different conditions: microhardness (a); engineering stress - engineering strain curves (b); strain hardening rate vs true strain (c) and Hall-Petch relation (d); in (d) data points were obtained during tension test of the alloy after 80% cold-rolling and further annealing for 1 h at 800-1100 °C.

Table 1
Tensile mechanical characteristics (YS - yield strength, UTS - ultimate tensile strength, TE - tensile elongation) of the $Al_5Nb_{24}Ti_{40}V_5Zr_{26}$ alloy after 80% cold rolling (CR) and CR + annealing at 800–1100 °C for 1 h.

Condition	E, GPa	YS, MPa	UTS, MPa	TE, %
CR	95.0	1200	1335	13.9
CR + annealing at 800 °C	96.5	835	880	26.7
CR + annealing at 900 °C	96.1	850	885	27.0
CR + annealing at 1000 °C	94.3	865	895	32.0
CR + annealing at 1100 °C	95.7	875	890	25.7

Annealing at 1100 °C changed the dislocation distribution after CR to $\varepsilon_{th} = 7\%$ considerably (Fig. 5 c, d). Dislocations localized in quite narrow (~100 nm) dislocation bands (DBs) with rather clear boundaries. Within the DBs crossing screw dislocations often formed networks (shown by arrows in Fig. 5c). All dislocations also possessed the $b = \pm a/2\langle 1\bar{1}1\rangle$ Burgers vector. Although DBs were often parallel to each other, many crossing DBs were also observed (Fig. 5 c). The spacing between the DBs was found to be ~250 nm; it worth noting that there were almost no dislocations in the areas between the DBs. When the goniometer angle met the $\boldsymbol{gb} = 0$ criteria, darker-gray straight strips were seen in the microstructure (Fig. 5d, upper part); these strips coincided with the DBs (Fig. 5d, lower part). It should be noted that the SAEDs taken from DBs

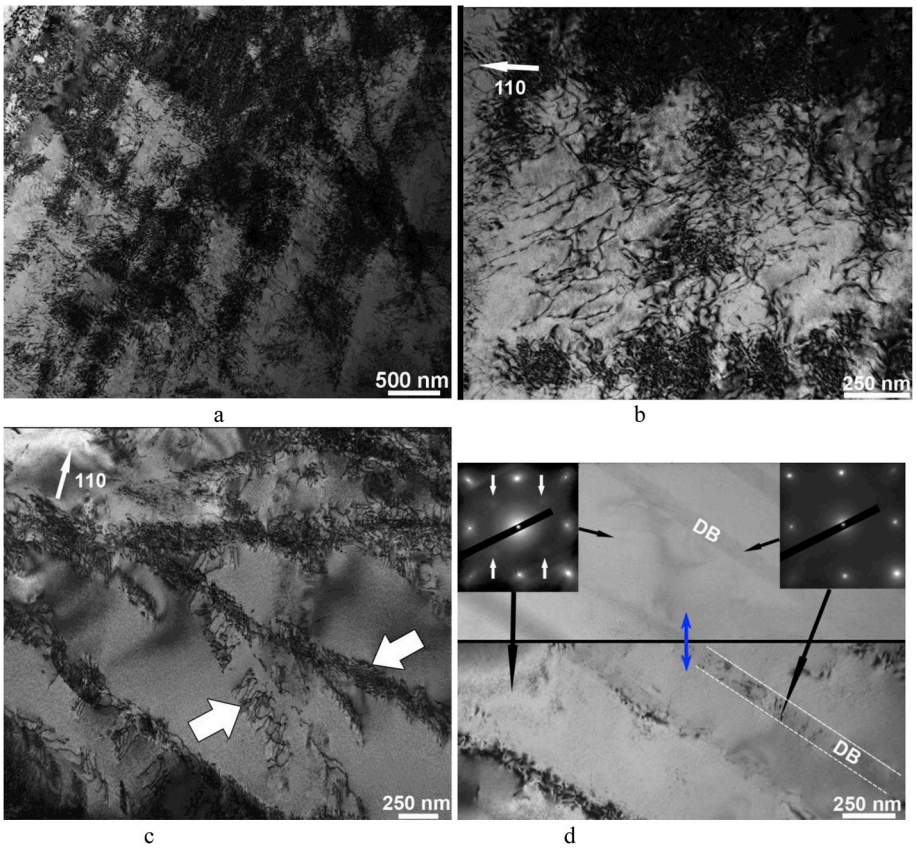

Fig. 5. TEM-bright field images of the $Al_5Nb_{24}Ti_{40}V_5Zr_{26}$ alloy CR to 7% thickness strain following recrystallization at 800 °C (a, b) or 1100 °C (c, d) for 1 h. The upper part of Fig. 5d was obtained under the $gb = 0$ condition; the lower part – in a random goniometer position.

have not revealed superlattice reflections in contrast to the areas between the DBs (inserts in Fig. 5d).

Typical SEM images of fracture surfaces obtained during tensile testing of the $Al_5Nb_{24}Ti_{40}V_5Zr_{26}$ alloy specimens at room temperature are shown in Fig. 6. Fracture surfaces of specimens recrystallized at 800 °C demonstrated typical dimple rupture (Fig. 6a). The size of dimples (2–6 μm) was found to be much smaller than the grain size in specimens (~19 μm); however the space between the Laves C14 phase particles (1–2 μm, Fig. 3a) was quite close to the dimples' size. In addition, many dimples contained hollows on their bottom thereby suggesting that the crack initiation was associated with the Laves phase particles. An increase in the recrystallization temperature till 1100 °C resulted in broadening (to 40–70 μm) and flattening of the dimples; many dimples contained low radial ridges. Crack nucleation at these temperatures can rarely be associated with second phase particles since only a few dimples contained hollows on the bottoms.

4. Discussion

The obtained results show that the introduced $Al_5Nb_{24}Ti_{40}V_5Zr_{26}$ HEA behaved in some respects like a typical gum metal, i.e. demonstrated high ductility, nearly horizontal engineering stress–strain curves due to lack of work hardening and relatively low Young's modulus (Fig. 4b, Table 1). However, this behavior can only be observed in recrystallized conditions while normally a gum behavior of the "classical" gum metals manifests itself after cold rolling (mechanical

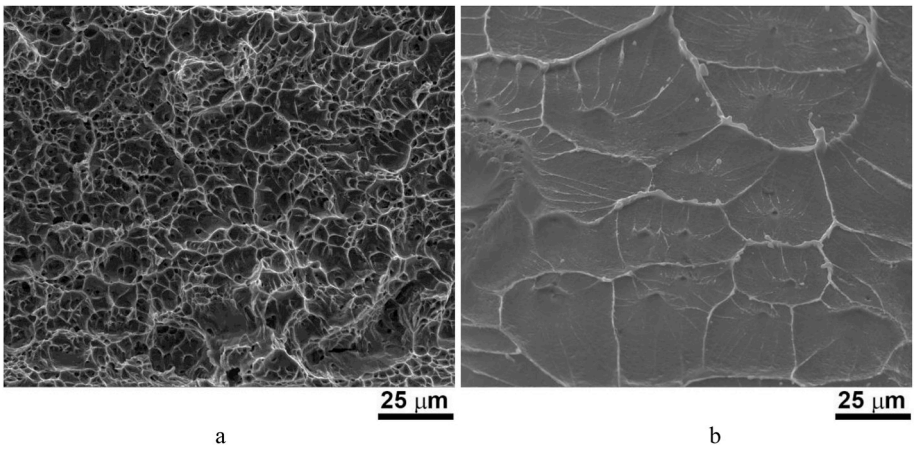

Fig. 6. Fracture surfaces of tensile $Al_5Nb_{24}Ti_{40}V_5Zr_{26}$ alloy specimens after CR to $\varepsilon_{th} = 80\%$ and further annealing for 1 h at 800 (a) or 1100 °C (b).

characteristics of the cold rolled $Al_5Nb_{24}Ti_{40}V_5Zr_{26}$ alloy were quite typical of a usual largely deformed metallic material (Fig. 4b)).

In addition the $Al_5Nb_{24}Ti_{40}V_5Zr_{26}$ alloy did not possess all inherent electronic parameters (in accordance with the classical gum metals definition [28]); only a compositional average valence number (e/a) of the HEA was appropriate (~4.24), while both the bond order (Bo) and "d" electron-orbital energy level (Md) were greater than the required ones (2.92 vs. 2.87 and 2.53 eV vs. 2.45 eV, respectively). Also, the composition of the HEA did not include 'essential' oxygen, while Al relates to neither IVa nor Va group.

Meanwhile, the observed gum-like mechanical behavior can definitely be ascribed to microstructural features of the alloy. One of the interesting findings was associated with the formation of a partially ordered bcc matrix (judging by the presence of weak superlattice reflections, Fig. 3b) as a result of post-deformation annealing at 1100 °C. Annealing at 800 °C did not lead to the formation of discernible superlattice reflections, however, small C14 Laves phase particles were observed in the microstructure (Fig. 3a). In the as-cast and cold rolled conditions, the alloy had the single disordered bcc phase structure (Fig. 1).

Deformation of the HEA with partially ordered structure was associated with the formation of DBs (Fig. 5); similar features were observed earlier in some Ti-based gum-like alloys [e.g. Ref. [37]]. However, in contrast to "classical" gum metals, where dislocation activity in giant faults was supposed to be quite limited [28], large shear deformation (and the corresponding gum-like behavior) in a Ti–Nb-based alloy was ascribed to the development of so-called dislocation channels in planes depleted of ω particles due to the local deformation-induced ω→β transformation [37]. Dislocation movement was confined to widely spaced planes which act like giant faults in gum metals. The formation of dislocation channels can also be observed in irradiated alloys in which these channels are devoid of irradiation-induced defects [38,39].

In our case, the dislocation channels formation should rather be ascribed to the local disordering of the bcc matrix in shear planes. Since an ordered lattice required higher resolved shear stress for slip [40], local disordering confines dislocation movement to narrow DBs (Fig. 3 c, d). Similar to the ω-enriched Ti–Nb-based alloy [37], dislocation channels in the recrystallized HEA promoted the low work hardening and large elongation in accordance with mechanisms known for gum metals [28–30]. Deformation-induced disordering in HEAs was earlier described for the $AlNbTiVZr_{0.5}$ alloy [41]; slip was also localized in shear bands (not so narrow though) resulting in a pronounced increase in compression ductility. Although the bcc matrix in metastable β titanium alloys can also have the B2 ordered lattice [42], the gum-like behavior in such alloys was not ascribed to matrix disordering.

B2 ordering in Al-containing RHEAs due to a strong interaction between atoms of Al and other elements composing the alloys was demonstrated earlier [41,43–48]. In the program $Al_5Nb_{24}Ti_{40}V_5Zr_{26}$ alloy, the atomic fraction of Al is quite low (5 at.%) that, most likely, prevents complete ordering. As a result partially ordered structure was attained only after annealing at 1100°C, meanwhile a decrease in the annealing temperature to 800 °C and corresponding decrease in diffusivity or a fast cooling rate from the melting temperature in the case of the as-cast condition resulted in the formation of a disordered structure or a structure which has undetectable level of ordering (Figs. 1a and 3a). It should be noted, however that qualitatively similar mechanical behavior of specimens recrystallized at both 800 and 1100 °C suggest some (quite weak though) ordering after annealing at 800 °C as well.

Basically almost the entirely single bcc phase structure of the alloy agrees with the equilibrium phase diagram constructed using the Thermo-Calc software (Fig. 7). However, neither the C14 Laves phase precipitation nor (partial) ordering of the bcc matrix were predicted by Thermo-Calc. Instead, a Zr_2Al phase with a composition close to the stoichiometric one and an Nb-rich bcc phase with the solvus temperature of ~600 °C can be expected in accordance with the equilibrium phase diagram. The lack of credibility of the existing thermodynamic databases, particularly in the B2 ordering prediction in the Al-containing RHEAs, due to an incomplete assessment of the binary/ternary phase diagrams was mentioned as a crucial issue in RHEAs development recently [5].

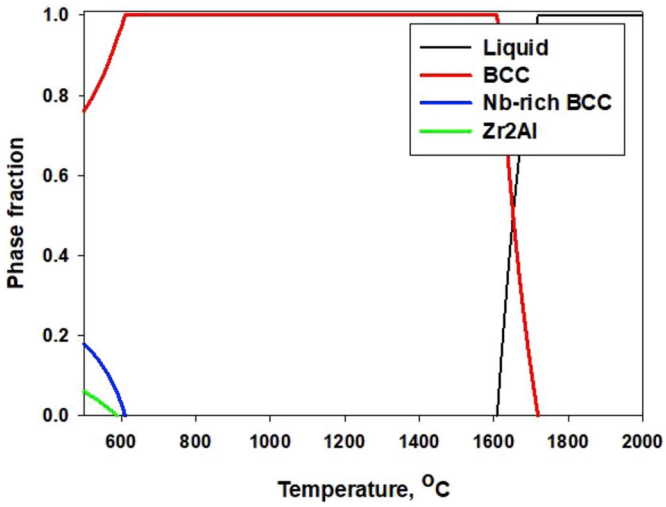

Fig. 7. Equilibrium phase diagram of the $Al_5Nb_{24}Ti_{40}V_5Zr_{26}$ alloy obtained using Thermo-Calc software.

Irrespective to the matrix condition, the dependence of grain size on annealing temperature (Fig. 2h) follows the general trend (i.e. the grain size increases while temperature rise); however, two distinct temperature intervals suggest some differences in the microstructure coarsening mechanisms. As it was mentioned above, one of the obvious factors of the sluggish grain growth at the lower temperatures is possibly related to the pinning effect from the C14 Laves phase particles; these particles were observed in the specimens annealed at 800 °C. It should be noted, however, that a very small amount of the Laves phase (less than 1% based on TEM images analysis) suggests rather low pinning pressure P_z according to the well-known Zener drag mechanism [49] $P_z = 3\gamma F_v/d$, where γ is the boundary surface energy per unit area; F_v and d are the fraction and size of dispersed particles, respectively.

An increase in grain growth kinetics at T > 900 °C can be associated not only with the second phase particles solution, however. Another possible reason is the transition from low to high boundary velocity due to the effect of solute on the boundary free volume and hence on the activation energy for solute diffusion. A model proposed by Cahn, Lucke and Stuwe [50,51] for dilute solid solutions predicts that in the high velocity regime, the activation energy for boundary migration should be rather high, similar to that for high purity material [52] thereby resulting in the intensive grain coarsening. This effect may be particularly pronounced in the case of complex-concentrated alloys containing five elements with rather a high amount.

Meanwhile, the alloy showed a quite unusual response of tensile strength on the annealing temperature: it became stronger with an increase in the annealing temperature and with the corresponding grain coarsening (Fig. 2) thereby resulting in what appears to be a negative Hall-Petch slope (Fig. 4d). Similar trend demonstrated microhardness as a function of the annealing temperature in the interval 700–1100 °C (Fig. 4d). The negative Hall-Petch slope was quite often reported for nanocrystalline condition of metallic materials [53–55]; however the proposed mechanisms of the inverse Hall-Petch effect can hardly be applied for the coarse-grained alloy examined in the current study. The observed deviation from the normal Hall-Petch behaviour can rather be associated with a more "ordered" structure of the alloy at the higher recrystallization temperature due to faster diffusivity (i.e. more time is needed at lower temperatures to obtain an ordered structure [56]). It should be noted however that basically the "degree of ordering" should decrease with temperature so that a less ordered structure is expected at

higher temperatures [56]; such the abnormal behavior obviously deserves further investigation. Meanwhile a higher "degree of ordering" restricted dislocations motion thereby making the inclination to gum-like behavior more evident. Particularly, deformation of a "weakly ordered" bcc matrix in specimens obtained by recrystallization at 800 °C resulted in more homogeneous dislocation distribution (wide and diffused dislocation bands can be seen in the deformed microstructure, however). This strengthening due to partial ordering appears to be stronger than the normal Hall-Petch softening due to grain coarsening. Also note that the hardness decreased with an increase in temperature in the range of 1100–1200 °C (Fig. 4a), thereby suggesting the normal Hall-Petch hardening most probably due to approaching the Curie temperature in this alloy and turning into a disordered condition.

The difference in the deformation mechanisms of specimens recrystallized at different temperatures can be clearly seen from the fracture surfaces of tensile specimens (Fig. 6). In the case of slightly ordered microstructure obtained by recrystallization at 800 °C the fracture surface is typical of a ductile alloy suggesting "normal" character of deformation and fracture. A more ordered (recrystallized at 1100 °C) structure fractured with the formation of flat-bottom extensive dimples. The bottom of these dimples can be produced by crack propagation along the dislocation channels while the crack nucleation is most likely associated with the sites of the dislocation channels crossing.

The obtained findings open new ways to tailor mechanical behavior properties of (R)HEAs with (partially) ordered microstructures by adjusting the "degree of ordering". It might be suggested that the compositional flexibility of (R)HEAs can provide ample opportunities for the new alloys development for a variety of structural and possibly functional applications [5,11,28], which can be further enriched by microstructural control via thermomechanical processing. Nevertheless, additional investigations are needed to establish reliably the composition-structure-properties relationship in such alloys in order to develop alloys suitable for potential practical usage.

5. Conclusions

In this study, the new $Al_5Nb_{24}Ti_{40}V_5Zr_{26}$ HEA was produced and its structure and mechanical properties were analyzed in different conditions. Following conclusions were drawn:

1) In the as-cast condition, the $Al_5Nb_{24}Ti_{40}V_5Zr_{26}$ alloy had a single bcc phase structure with grains of 80 μm. Cold rolling and subsequent annealing at 700-1200 °C resulted in recrystallization of the heavily deformed bcc matrix. A small fraction of tiny C14 type Laves phase particles was found after annealing at 800 °C. In turn, partial B2 ordering of the matrix phase was found after annealing at 1100°C. The presence of the second phase particles and operating of a high boundary velocity regime at the lower and higher temperatures, respectively, resulted in a two-stage relationship between the bcc recrystallized grain size and annealing temperature with the inflection point at ~900 °C.
2) The cold rolled to a total thickness strain 80% alloy demonstrated typical of deformed metals tensile behavior with a short hardening stage and early necking. Meanwhile, the annealed alloys demonstrated high yield strength with limited strain hardening capacity and simultaneously pronounced uniform elongation, i.e. behaved essentially like Ti-based gum metals. Moreover, the yield strength and hardness of the alloy increased with an increase in the annealing temperature in the 700–1100 °C interval and corresponding bcc grain growth.
3) Strong strain localization in dislocation bands (DBs) was found during deformation of the alloy annealed at 1100 °C. TEM examinations have not revealed superlattice reflections from the DBs while they were found in the areas between DBs. Dislocation channeling in DBs was supposed to be the reason for the gum-like mechanical behavior manifestation. Much more uniform dislocation substructure was observed during deformation of the alloy annealed at 800°C, most probably due to less "ordered" structure. Different "degree of ordering" depending on the annealing temperature was also supposed to be the main reason for increased strength of the alloys with larger grain sizes, contrary to the Hall-Petch mechanism.

Data availability statement

The raw/processed data required to reproduce these findings cannot be shared at this time as the data also forms part of an ongoing study.

Declaration of competing interest

None.

Acknowledgement

The authors gratefully acknowledge the financial support from the Russian Science Foundation Grant no. 19-79-30066. The authors are grateful to the personnel of the Joint Research Center, "Technology and Materials", Belgorod National Research University, for their assistance.

Appendix A. Supplementary data

Supplementary data to this article can be found online at https://doi.org/10.1016/j.intermet.2019.106652.

References

[1] J.W. Yeh, S.K. Chen, S.J. Lin, J.Y. Gan, T.S. Chin, T.T. Shun, C.H. Tsau, S.Y. Chang, Nanostructured high-entropy alloys with multiple principal elements: novel alloy design concepts and outcomes, Adv. Eng. Mater. 6 (2004) 299–303+274, https://doi.org/10.1002/adem.200300567.
[2] Y. Zhang, T.T. Zuo, Z. Tang, M.C. Gao, K.A. Dahmen, P.K. Liaw, Z.P. Lu, Microstructures and properties of high-entropy alloys, Prog. Mater. Sci. 61 (2014) 1–93, https://doi.org/10.1016/j.pmatsci.2013.10.001.
[3] B. Gludovatz, A. Hohenwarter, D. Catoor, E.H. Chang, E.P. George, R.O. Ritchie, A fracture-resistant high-entropy alloy for cryogenic applications, Science 345 (80-) (2014) 1153–1158, https://doi.org/10.1126/science.1254581.
[4] D.B. Miracle, O.N. Senkov, A critical review of high entropy alloys and related concepts, Acta Mater. 122 (2017) 448–511, https://doi.org/10.1016/j.actamat.2016.08.081.
[5] O.N. Senkov, D.B. Miracle, K.J. Chaput, J.-P. Couzinie, Development and exploration of refractory high entropy alloys—a review, J. Mater. Res. (2018) 1–37, https://doi.org/10.1557/jmr.2018.153.
[6] Z. Li, K.G. Pradeep, Y. Deng, D. Raabe, C.C. Tasan, Metastable high-entropy dual-phase alloys overcome the strength–ductility trade-off, Nature 534 (2016) 227, https://doi.org/10.1038/nature17981.
[7] F. Otto, Y. Yang, H. Bei, E.P. George, Relative effects of enthalpy and entropy on the phase stability of equiatomic high-entropy alloys, Acta Mater. 61 (2013) 2628–2638, https://doi.org/10.1016/J.ACTAMAT.2013.01.042.
[8] M. Laurent-Brocq, L. Perrière, R. Pirès, Y. Champion, From high entropy alloys to diluted multi-component alloys: range of existence of a solid-solution, Mater. Des. 103 (2016) 84–89, https://doi.org/10.1016/j.matdes.2016.04.046.
[9] O.N. Senkov, J.D. Miller, D.B. Miracle, C. Woodward, Accelerated exploration of multi-principal element alloys with solid solution phases, Nat. Commun. 6 (2015), https://doi.org/10.1038/ncomms7529.
[10] D.B. Miracle, J.D. Miller, O.N. Senkov, C. Woodward, M.D. Uchic, J. Tiley, Exploration and development of high entropy alloys for structural applications, Entropy 16 (2014) 494–525, https://doi.org/10.3390/e16010494.
[11] S. Gorsse, D.B. Miracle, O.N. Senkov, Mapping the world of complex concentrated alloys, Acta Mater. 135 (2017) 177–187, https://doi.org/10.1016/j.actamat.2017.06.027.
[12] F. Otto, A. Dlouhý, C. Somsen, H. Bei, G. Eggeler, E.P. George, The influences of temperature and microstructure on the tensile properties of a CoCrFeMnNi high-entropy alloy, Acta Mater. 61 (2013) 5743–5755, https://doi.org/10.1016/j.actamat.2013.06.018.
[13] B. Gludovatz, A. Hohenwarter, K.V.S. Thurston, H. Bei, Z. Wu, E.P. George, R. O. Ritchie, Exceptional damage-tolerance of a medium-entropy alloy CrCoNi at cryogenic temperatures, Nat. Commun. (2016), https://doi.org/10.1038/ncomms10602.
[14] A.J. Zaddach, R.O. Scattergood, C.C. Koch, Tensile properties of low-stacking fault energy high-entropy alloys, Mater. Sci. Eng. A 636 (2015) 373–378, https://doi.org/10.1016/j.msea.2015.03.109.
[15] N. Stepanov, M. Tikhonovsky, N. Yurchenko, D. Zyabkin, M. Klimova, S. Zherebtsov, A. Efimov, G. Salishchev, Effect of cryo-deformation on structure

and properties of CoCrFeNiMn high-entropy alloy, Intermetallics 59 (2015), https://doi.org/10.1016/j.intermet.2014.12.004.
[16] T.M. Smith, M.S. Hooshmand, B.D. Esser, F. Otto, D.W. Mccomb, E.P. George, M. Ghazisaeidi, M.J. Mills, Atomic-scale characterization and modeling of 60°dislocations in a high-entropy alloy, Acta Mater. 110 (2016) 352–363, https://doi.org/10.1016/j.actamat.2016.03.045.
[17] S.I. Rao, C. Woodward, T.A. Parthasarathy, O. Senkov, Atomistic simulations of dislocation behavior in a model FCC multicomponent concentrated solid solution alloy, Acta Mater. 134 (2017) 188–194, https://doi.org/10.1016/J.ACTAMAT.2017.05.071.
[18] M.S. Lucas, G.B. Wilks, L. Mauger, J.A. Muñoz, O.N. Senkov, E. Michel, J. Horwath, S.L. Semiatin, M.B. Stone, D.L. Abernathy, E. Karapetrova, Absence of long-range chemical ordering in equimolar FeCoCrNi, Appl. Phys. Lett. 100 (2012) 251907, https://doi.org/10.1063/1.4730327.
[19] C. Niu, A.J. Zaddach, A.A. Oni, X. Sang, J.W. Hurt, J.M. LeBeau, C.C. Koch, D. L. Irving, Spin-driven ordering of Cr in the equiatomic high entropy alloy NiFeCrCo, Appl. Phys. Lett. 106 (2015) 161906, https://doi.org/10.1063/1.4918996.
[20] Q.-J. Li, H. Sheng, E. Ma, Strengthening in multi-principal element alloys with local-chemical-order roughened dislocation pathways, Nat. Commun. 10 (2019) 3563, https://doi.org/10.1038/s41467-019-11464-7.
[21] O.N. Senkov, J.M. Scott, S.V. Senkova, D.B. Miracle, C.F. Woodward, Microstructure and room temperature properties of a high-entropy TaNbHfZrTi alloy, J. Alloy. Comp. 509 (2011) 6043–6048, https://doi.org/10.1016/j.jallcom.2011.02.171.
[22] O.N. Senkov, J.M. Scott, S.V. Senkova, F. Meisenkothen, D.B. Miracle, C. F. Woodward, Microstructure and elevated temperature properties of a refractory TaNbHfZrTi alloy, J. Mater. Sci. 47 (2012) 4062–4074, https://doi.org/10.1007/s10853-012-6260-2.
[23] J.-P. Couzinié, L. Lilensten, Y. Champion, G. Dirras, L. Perrière, I. Guillot, On the room temperature deformation mechanisms of a TiZrHfNbTa refractory high-entropy alloy, Mater. Sci. Eng. A 645 (2015) 255–263, https://doi.org/10.1016/j.msea.2015.08.024.
[24] L. Lilensten, J.-P. Couzinié, L. Perrière, A. Hocini, C. Keller, G. Dirras, I. Guillot, Study of a bcc multi-principal element alloy: tensile and simple shear properties and underlying deformation mechanisms, Acta Mater. 142 (2018) 131–141.
[25] S. Maiti, W. Steurer, Structural-disorder and its effect on mechanical properties in single-phase TaNbHfZr high-entropy alloy, Acta Mater. 106 (2016) 87–97.
[26] Z. Lei, X. Liu, Y. Wu, H. Wang, S. Jiang, S. Wang, X. Hui, Y. Wu, B. Gault, P. Kontis, D. Raabe, L. Gu, Q. Zhang, H. Chen, H. Wang, J. Liu, K. An, Q. Zeng, T.-G. Nieh, Z. Lu, Enhanced strength and ductility in a high-entropy alloy via ordered oxygen complexes, Nature 563 (2018) 546–550, https://doi.org/10.1038/s41586-018-0685-y.
[27] O.N. Senkov, S.L. Semiatin, Microstructure and properties of a refractory high-entropy alloy after cold working, J. Alloy. Comp. 649 (2015) 1110–1123, https://doi.org/10.1016/j.jallcom.2015.07.209.
[28] T. Saito, T. Furuta, J.-H. Hwang, S. Kuramoto, K. Nishino, N. Suzuki, R. Chen, A. Yamada, K. Ito, Y. Seno, T. Nonaka, H. Ikehata, N. Nagasako, C. Iwamoto, Y. Ikuhara, T. Sakuma, Multifunctional alloys obtained via a dislocation-free plastic deformation mechanism, Science 300 (2003) 464–467, https://doi.org/10.1126/science.1081957.
[29] M.Y. Gutkin, T. Ishizaki, S. Kuramoto, I.A. Ovid'ko, N.V. Skiba, Giant faults in deformed gum metal, Int. J. Plast. 24 (2008) 1333–1359, https://doi.org/10.1016/J.IJPLAS.2007.09.009.
[30] E. Plancher, C.C. Tasan, S. Sandloebes, D. Raabe, On dislocation involvement in Ti–Nb gum metal plasticity, Scr. Mater. 68 (2013) 805–808, https://doi.org/10.1016/J.SCRIPTAMAT.2013.01.034.
[31] R.J. Talling, R.J. Dashwood, M. Jackson, D. Dye, On the mechanism of superelasticity in Gum metal, Acta Mater. 57 (2009) 1188–1198, https://doi.org/10.1016/J.ACTAMAT.2008.11.013.
[32] T. Li, J.W. Morris, N. Nagasako, S. Kuramoto, D.C. Chrzan, "Ideal" engineering alloys, Phys. Rev. Lett. 98 (2007) 105503, https://doi.org/10.1103/PhysRevLett.98.105503.
[33] M. Tahara, H.Y. Kim, T. Inamura, H. Hosoda, S. Miyazaki, Lattice modulation and superelasticity in oxygen-added β-Ti alloys, Acta Mater. 59 (2011) 6208–6218, https://doi.org/10.1016/J.ACTAMAT.2011.06.015.
[34] Y. Yang, P. Castany, M. Cornen, F. Prima, S.J. Li, Y.L. Hao, T. Gloriant, Characterization of the martensitic transformation in the superelastic Ti–24Nb–4Zr–8Sn alloy by in situ synchrotron X-ray diffraction and dynamic mechanical analysis, Acta Mater. 88 (2015) 25–33, https://doi.org/10.1016/J.ACTAMAT.2015.01.039.
[35] Q. Liang, Y. Zheng, D. Wang, Y. Hao, R. Yang, Y. Wang, H.L. Fraser, Nano-scale structural non-uniformities in gum like Ti-24Nb-4Zr-8Sn metastable β-Ti alloy, Scr. Mater. 158 (2019) 95–99, https://doi.org/10.1016/J.SCRIPTAMAT.2018.08.043.
[36] C.-C.C. Juan, M.-H.H. Tsai, C.-W.W. Tsai, W.-L.L. Hsu, C.-M.M. Lin, S.-K.K. Chen, S.-J.J. Lin, J.-W.W. Yeh, Simultaneously increasing the strength and ductility of a refractory high-entropy alloy via grain refining, Mater. Lett. 184 (2016) 200–203, https://doi.org/10.1016/j.matlet.2016.08.060.
[37] M.J. Lai, C.C. Tasan, D. Raabe, Deformation mechanism of ω-enriched Ti–Nb-based gum metal: dislocation channeling and deformation induced ω–β transformation, Acta Mater. 100 (2015) 290–300, https://doi.org/10.1016/J.ACTAMAT.2015.08.047.
[38] A. Luft, Microstructural processes of plastic instabilities in strengthened metals, Prog. Mater. Sci. 35 (1991) 97–204, https://doi.org/10.1016/0079-6425(91)90002-B.
[39] T. Diaz de la Rubia, H.M. Zbib, T.A. Khraishi, B.D. Wirth, M. Victoria, M.J. Caturla, Multiscale modelling of plastic flow localization in irradiated materials, Nature 406 (2000) 871–874, https://doi.org/10.1038/35022544.
[40] M.A. Meyers, K.K. Chawla, Mechanical Behavior of Materials, Cambridge University Press, 2009.
[41] N.Y. Yurchenko, N.D. Stepanov, S.V. Zherebtsov, M.A. Tikhonovsky, G. A. Salishchev, Structure and mechanical properties of B2 ordered refractory AlNbTiVZrx (x = 0–1.5) high-entropy alloys, Mater. Sci. Eng. A 704 (2017) 82–90, https://doi.org/10.1016/j.msea.2017.08.019.
[42] J.-P. Liu, Y.-D. Wang, Y.-L. Hao, Y. Wang, Z.-H. Nie, D. Wang, Y. Ren, Z.-P. Lu, J. Wang, H. Wang, X. Hui, N. Lu, M.J. Kim, R. Yang, New intrinsic mechanism on gum-like superelasticity of multifunctional alloys, Sci. Rep. 3 (2013) 2156, https://doi.org/10.1038/srep02156.
[43] Y. Qiu, Y.J. Hu, A. Taylor, M.J. Styles, R.K.W. Marceau, A.V. Ceguerra, M. A. Gibson, Z.K. Liu, H.L. Fraser, N. Birbilis, A lightweight single-phase AlTiVCr compositionally complex alloy, Acta Mater. 123 (2017) 115–124, https://doi.org/10.1016/j.actamat.2016.10.037.
[44] W. Chen, Q.H. Tang, H. Wang, Y.C. Xie, X.H. Yan, P.Q. Dai, Microstructure and mechanical properties of a novel refractory AlNbTiZr high-entropy alloy, Mater. Sci. Technol. (2018) 1–7, https://doi.org/10.1080/02670836.2018.1446267.
[45] N.D. Stepanov, N.Y. Yurchenko, A.O. Gridneva, S.V. Zherebtsov, Y.V. Ivanisenko, G.A. Salishchev, Structure and hardness of B2 ordered refractory AlNbTiVZr0.5 high entropy alloy after high-pressure torsion, Mater. Sci. Eng. A 716 (2018) 308–315, https://doi.org/10.1016/j.msea.2018.01.061.
[46] J.K. Jensen, B.A. Welk, R.E.A. Williams, J.M. Sosa, D.E. Huber, O.N. Senkov, G. B. Viswanathan, H.L. Fraser, Characterization of the microstructure of the compositionally complex alloy Al1Mo0.5Nb1Ta0.5Ti1Zr1, Scr. Mater. 121 (2016) 1–4, https://doi.org/10.1016/j.scriptamat.2016.04.017.
[47] O.N. Senkov, J.K. Jensen, A.L. Pilchak, D.B. Miracle, H.L. Fraser, Compositional variation effects on the microstructure and properties of a refractory high-entropy superalloy AlMo0.5NbTa0.5TiZr, Mater. Des. 139 (2018) 498–511, https://doi.org/10.1016/j.matdes.2017.11.033.
[48] V. Soni, O.N. Senkov, B. Gwalani, D.B. Miracle, R. Banerjee, Microstructural design for improving ductility of an initially brittle refractory high entropy alloy, Sci. Rep. (2018) 1, https://doi.org/10.1038/s41598-018-27144-3.
[49] G.S. Rohrer, Introduction to grains, phases, and interfaces—an interpretation of microstructure, Trans. AIME 175 (1948) 15–51, https://doi.org/10.1007/s11661-010-0215-5. C.S. Smith, Metall. Mater. Trans. A. 41 (2010) 1063–1100.
[50] J.W. Cahn, The impurity-drag effect in grain boundary motion, Acta Metall. 10 (1962) 789–798, https://doi.org/10.1016/0001-6160(62)90092-5.
[51] K. Lücke, H.P. Stüwe, On the theory of impurity controlled grain boundary motion, Acta Metall. 19 (1971) 1087–1099, https://doi.org/10.1016/0001-6160(71)90041-1.
[52] F.J. Humphreys, M. Hatherly, Recrystallization and Related Annealing Phenomena, Elsevier, 2004.
[53] G.W. Nieman, J.R. Weertman, R.W. Siegel, Microhardness of nanocrystalline palladium and copper produced by inert-gas condensation, Scr. Metall. 23 (1989) 2013–2018, https://doi.org/10.1016/0036-9748(89)90223-8.
[54] A.H. Chokshi, A. Rosen, J. Karch, H. Gleiter, On the validity of the hall-petch relationship in nanocrystalline materials, Scr. Metall. 23 (1989) 1679–1683, https://doi.org/10.1016/0036-9748(89)90342-6.
[55] C.E. Carlton, P.J. Ferreira, What is behind the inverse Hall–Petch effect in nanocrystalline materials? Acta Mater. 55 (2007) 3749–3756, https://doi.org/10.1016/J.ACTAMAT.2007.02.021.
[56] H. Sato, R. Kikuchi, Kinetics of order-disorder transformations in alloys, Acta Metall. 24 (1976) 797–809, https://doi.org/10.1016/0001-6160(76)90046-8.